



[biblio.ugent.be](https://biblio.ugent.be)

The UGent Institutional Repository is the electronic archiving and dissemination platform for all UGent research publications. Ghent University has implemented a mandate stipulating that all academic publications of UGent researchers should be deposited and archived in this repository. Except for items where current copyright restrictions apply, these papers are available in Open Access.

This item is the archived peer-reviewed author-version of:

Validation of a coupled heat, vapour and liquid moisture transport model for porous materials implemented in CFD

Marnix Van Belleghem, Marijke Steeman, Hans Janssen, Arnold Janssens and Michel De Paepe

In: Building and Environment, 81, pp. 340-353, 2014.

**To refer to or to cite this work, please use the citation to the published version:**

Van Belleghem M., Steeman M., Janssen H., Janssens A., De Paepe M. (2014) Validation of a coupled heat, vapour and liquid moisture transport model for porous materials implemented in CFD. Building and Environment 81, 340-353. doi: 10.1016/j.buildenv.2014.06.024

# Validation of a coupled heat, vapour and liquid moisture transport model for porous materials implemented in CFD

M. Van Belleghem<sup>1</sup>, M. Steeman<sup>2</sup>, H. Janssen<sup>3</sup>, A. Janssens<sup>4</sup> and M. De Paepe<sup>1</sup>

<sup>1</sup> Ghent University, Department of Flow, Heat and Combustion Mechanics, Sint-Pietersnieuwstraat 40, B-9000 Gent, Belgium

<sup>2</sup> Ghent University, Department of Industrial Technology and Construction, Valentin Vaerwijckweg 1, B-9000 Gent, Belgium

<sup>3</sup> Building Physics Section, Department of Civil Engineering, KU Leuven, Kasteelpark Arenberg 40, B-3000 Leuven, Belgium

<sup>4</sup> Ghent University, Department of Architecture and Urban Planning, Jozef Plateaustraat 22, B-9000 Gent, Belgium

Corresponding author: Marnix Van Belleghem

Tel +3292643289 / Fax +3292643575

Email: marnix.vanbelleghem@UGent.be

## Keywords

Heat and moisture transfer, HAM, CFD, Porous material, Drying

## Abstract

Moisture-related damage is an important issue when looking at the performance of building envelopes. In order to accurately predict the moisture behaviour of building components, building designers can resort to Heat, Air and Moisture (HAM) models. In this paper a newly developed heat and mass transfer model that is implemented in a 3D finite volume solver, Fluent®, is presented. This allows a simultaneous modelling approach of both the convective conditions surrounding a porous material and the heat and moisture transport in the porous material governed by diffusion. Unlike most HAM models that often confine to constant convective transport coefficients it is now possible to better predict these convective boundary conditions. An important application of the model is the convective drying of porous building materials. Especially during the first drying stage, the drying rate is determined by the convective boundary conditions. The model was validated against a convective drying experiment from literature, in which a saturated ceramic brick sample is dried by flowing dry air over one side of the sample surface. Temperature and relative humidity measurements at different depths in the sample, moisture distribution profiles and mass loss measurements were compared with simulation results. An overall good agreement between the coupled model and the experiments was found, however, the model predicted the constant drying rate period better than the falling rate period. This was improved by adjusting the material properties. The adjustment of the material properties was supported by neutron radiography measurements.

## Nomenclature

Symbol	Description	Unit
$c_p$	Specific heat	J/kgK
C	Specific heat capacity	J/kgK
$C_b$	Stefan Boltzmann constant ( $5.67 \times 10^{-8} \text{ W/m}^2\text{K}^4$ )	-
$D_{va}$	Diffusivity of water vapour in air	$\text{m}^2/\text{s}$
E	Total energy	J
g	Moisture flux	$\text{kg}/\text{m}^2\text{s}$

---

$h$	Specific enthalpy	J/kg
$h$	Heat transfer coefficient (convection and radiation)	W/m <sup>2</sup> K
$h^T$	Convective heat transfer coefficient	W/m <sup>2</sup> K
$h_m^Y$	Convective mass transfer coefficient	s/m
$K_l$	Liquid permeability	s
$L$	Latent heat	J/kg
$P$	Pressure	Pa
$p_v$	Partial vapour pressure	Pa
$p_c$	Capillary pressure	Pa
$q$	Heat Flux	W/m <sup>2</sup>
RH	Relative humidity	-
$R_v$	Specific gas constant of water vapour	J/kgK
$T$	Temperature	K
$v$	Velocity	m/s
$w$	Moisture content	kg/m <sup>3</sup>
$Y$	Mass fraction	kg/kg
<i>Greek symbols</i>		
$\delta$	Diffusion coefficient	s
$\varepsilon$	Emissivity	-
$\lambda$	Heat conductivity	W/mK
$\mu$	Water vapour diffusion resistance factor	-
$\rho$	Density	kg/m <sup>3</sup>
$\psi_0$	Open porosity	-
<i>Subscripts</i>		
cap	Capillary	
s	Surface	
l	Liquid	
mat	Material	
op	Operating	

---

---

rad	Radiation
ref	Reference
sat	Saturation
v	Vapour
<i>Acronyms</i>	
BES	Building Energy Simulations
CFD	Computational Fluid Dynamics
HAM	Heat, Air and Moisture

---

## 1. Introduction

During the last decades the requirements for quality of buildings and its envelopes have drastically increased. Where before the main function of a building was to protect people from outside weather conditions, nowadays building users demand high-performance buildings with comfortable temperature and humidity levels without excessive energy use. However, damage to the building envelope can reduce the building performance to a great extent. This damage is often moisture-related and may affect the indoor comfort and indoor air quality [1,2], energy efficiency [3,4], human health and durability [5]. In order to prevent moisture-related damage, building designers need reliable predictive tools which can help them to design high performance building envelopes.

Modelling tools describing the moisture behaviour of buildings and its envelopes are very useful to predict and evaluate moisture related problems. HAM (Heat, Air and Moisture) models are frequently being used to solve the combined transport of heat and moisture in building components. Nowadays, a wide variety of modelling tools are available [6].

These HAM models can be combined with other models to improve their performance. Examples are combined BES-HAM models [7,8] and CFD-HAM models [9e11]. In BES-HAM models, HAM is combined with building energy simulations to improve the prediction of building energy performance by including the hygroscopic behaviour of building materials. In combined CFD-HAM models, HAM is coupled with computational fluid dynamics to better incorporate the coupled effect of convective transport of heat and moisture in the air and in the porous material. Steeman et al. [9] developed a coupled CFD-HAM model for the assessment of moisture-related damage in hygroscopic materials. By implementing a detailed HAM model into an existing CFD solver (Fluent®) he was able to model the heat and moisture transport in the air and porous material simultaneously. The coupled model was validated using climate chamber experiments [12]. However, Steeman only modelled vapour diffusion as a transport mechanism in the porous material. With the model, it was possible to predict the microclimate around valuable objects such as paintings. Other attempts of combining CFD and HAM can be found in Mortensen et al. [13] and Defraeye et al. [14]. Defraeye applied an external coupling procedure and used a separate CFD and HAM model which were then combined by transferring and setting the boundary conditions from one model to the other.

These recent attempts to combine existing HAM models with CFD showed to be promising. They allow a more detailed and accurate modelling of the influence of convection on the heat and moisture transport in porous materials. However the development of these hygrothermal models is still on-going.

In this paper, a newly developed CFD-HAM model is described in which the heat and moisture transport equations for porous materials are implemented into a commercial available CFD solver, Fluent®. The model includes vapour as well as liquid water transport. Since it is implemented into an existing CFD solver it is easier to combine it with convective transport in the air surrounding the porous material. The model is therefore specifically suited to study cases where convective boundary conditions are dominant or where the interaction of transport in the air and transport in the porous material is important. A few examples of such cases are the effect of microclimates on historical artefacts [9], drying of building materials during production [15], drying of building envelopes after rain, evaporative cooling of buildings and street canyons [16], etc.

Before this model can be applied to actual case studies, it is first extensively validated. This paper will focus on this model validation. It will highlight some important aspects when modelling combined heat and moisture transport in porous materials, such as numerical implementation of boundary conditions, the importance of correct material properties and the choice of the driving potentials to be used. In a follow-up paper a case study will be elaborated [17].

## **2. State of the art in convective drying modelling**

In buildings, drying almost always occurs by convection. If the partial vapour pressure of the air is lower than the vapour pressure at the surface of a porous material, moisture will be transferred to the air and is transported away from the surface by the moving air.

Fig. 1 qualitatively depicts a typical drying rate curve of a capillary active hygroscopic material. At first, free moisture at the material surface evaporates from the surface and the drying rate is determined by the diffusion rate of water vapour into the surrounding air. During this constant drying rate period (CRP), moisture is transported from the inside of the porous material to the surface by capillary forces. As long as this transport can sustain the evaporation rate from the surface, the drying rate will remain constant.

If the moisture content reaches a critical level at which the moisture can no longer reach the surface at a sufficient rate, further drying will cause the surface relative humidity to drop below 100%. This is the start of the second drying stage or the falling rate period (FRP). The drying rate is determined by the internal moisture diffusion transport as a result of moisture concentration gradients in the material. As the material dries out, moisture movement decreases further and consequently the drying rate drops. The drying rate continues to fall until the moisture content inside the material is in equilibrium with the surrounding air. At that point the drying rate becomes zero and drying stops.

During the CRP the temperature at the surface drops close to the wet bulb temperature. If the starting temperature in the material is higher than the wet bulb temperature, the temperature will start to drop and accordingly the drying rate will also drop. On the other hand, when initially the temperature is lower than the wet bulb temperature, the material temperature starts to rise and so will the drying rate (dashed lines in Fig. 1).

In literature, a wide range of drying models is available. A distinction can be made between analytical and numerical models. In the following sections, a short overview is given of the state-of-the-art modelling approaches for combined heat and mass transport during convective drying in air.

### **2.1. Analytical modelling**

Analytical models such as 1D models assuming constant diffusivity, only apply to simplified drying cases. The applied boundary conditions are fixed temperature and humidity (Dirichlet boundary conditions), fixed fluxes (Neumann boundary conditions) or fixed transfer coefficients (Robin boundary conditions).

Milly [18] and more recently Abahri et.al. [19] developed an analytical solution for a coupled 1D heat and moisture transfer problem. Their models are however limited to Dirichlet and Neumann boundary conditions and are not sufficient when convective drying is studied. To model convective drying, at

least a Robin boundary condition is needed. If more complex boundary conditions are present such as spatially or even temporally varying boundary conditions, 1D analytical models are no longer sufficient.

Moreover, most convective drying processes do not allow simplifications like constant diffusivity. For most materials and in particular building materials, the diffusivity shows a strong non-linear behaviour as function of moisture content. In literature, some solutions to non-linear diffusivity can be found, e.g. Landman et al. [20] looked at the drying process of a brick.

Analytical solutions can thus only be used when simple geometrical configurations, material properties and boundary conditions apply. As soon as more complex and realistic boundary conditions are to be solved, as is often the case in the building context, analytical models no longer work. Building components are generally composed of multiple layers, inserting strong heterogeneity into the problem. At the same time the boundary conditions are not fixed in time and space, resulting in temporal and spatial distributions of temperature and moisture. Consequently, it is not feasible to solve all coupled heat and mass transport problems, especially drying problems, by simple 1D analytical approaches.

## **2.2. Numerical modelling: predetermined transfer coefficients**

Numerical models can be used to solve complex 2D or 3D configurations and to overcome some of the issues related to analytical models. To incorporate the influence of airflow properties on convective drying without modelling the convection in the air simultaneously with the transport in the porous material, researchers often resort to transfer coefficients.

The simplest approach is using constant (averaged) transfer coefficients. Most HAM models use this method [7,21,22]. Berger et al. [23] were able to study drying phenomena using a 1D finite difference model with constant heat and mass transfer coefficients as boundary conditions. Furthermore, their study showed that the convective transfer coefficient determined the drying rate during the CRP. During the FRP the drying rate is mostly determined by the internal transport properties and the impact of the convective transfer coefficients is negligible. Although these conclusions were derived with a simplified 1D model, they can be generally applied.

The use of constant transfer coefficients is however only valid if the flow is fully developed which is often not the case even for simple geometrical conditions. The presence of developing boundary layers or complex geometries with leading edge effects, vortex shedding, reattachment and stagnation zones may lead to large distributions of transfer coefficient values along the surface. Furthermore, several researchers found that the leading edge effect has a significant impact especially during the CRP [24 - 26]. E.g. Masmoudi et al. [24] found that simplifying drying problems to 1D problems is not generally applicable because the leading edge effect will be significant if the sample size is not clearly larger than the mass or temperature boundary leading edge zones. Also Shokouhmand et al. [26] found that the leading edge effect was crucial in the determination of the drying time.

A more accurate and detailed study of the convective drying process is possible when spatially varying transfer coefficients are used. These coefficients can be derived from analytical solutions for simple cases or from CFD solutions when more complex geometries and flow conditions are present.

The most common approach to determine the transfer coefficients from CFD is by solving the flow with the assumption of constant boundary temperature and mass fraction [25, 27]. For convective drying this approach is only strictly applicable during the CRP when the surface temperature is almost constant and near to the wet bulb temperature and the surface mass fraction corresponds with the saturation mass fraction for that temperature. Nevertheless this approach is often used with reasonably good results.

## **2.3. Numerical modelling: coupling HAM with CFD**

In the drying models discussed up till now the flow field is assumed to be steady and solved separately from the material model [28]. This can be justified if the heat and mass transfers are moderate and if the fluxes through the solid-fluid interface do not disturb the velocity field. The variations in air density

are ignored and air is considered incompressible. The heat and mass transfer coefficients are then determined by solving transport in the air only once and assuming constant boundary conditions at the material surface (temperature and moisture concentration).

When the surface of a porous material starts to dry out, large temperature and moisture distributions along the surface can occur. Strictly speaking, the assumption of constant boundary conditions is then no longer valid. For instance Masmoudi et al. [24] showed the effect of heterogeneities in the moisture content distribution at the surface (such as dry zones) on the transfer at the interface. The transfer coefficients clearly showed dependency on the surface moisture distribution. Similar results were found by Defraeye et al. [14].

To implement these effects of varying transfer coefficients, it is possible to use CFD as a tool to predict the transfer coefficients. When CFD and HAM are combined, the heat and mass transfer in the air and the porous material can be solved simultaneously, without the need of estimated transfer coefficients. Such models are referred to in literature as conjugate models. Defraeye et al. [29] gives a good overview of recent developments in this field of modelling.

An early attempt to develop a coupled model was done by Amir et al. [30]. Amir et al. developed an implicit finite difference model that simultaneously solved the set of equations for a laminar boundary layer and a porous thick slab immersed in the boundary layer. The laminar velocity boundary layer was considered to be steady and independent of heat and moisture. This allowed them to solve the velocity boundary layer separately from the heat and moisture transport equation. The heat and moisture transport equation in the boundary layer and in the porous material were then solved simultaneously and coupled.

Zeghmami et al. [31] continued the work of Amir et al. by extending the model to include transient laminar natural convection. The Boussinesq approximation was assumed for the boundary layer momentum equation. Dolinskiy et al. [32] employed a similar model to simulate the drying of a thick slab for the initial period of drying (moisture content exceeded the maximum sorption moisture content). The authors found that the analogy between heat and mass transfer, often employed to predict transfer coefficients, was not applicable. This was due to the fact that, for maintaining the analogy, not only the differential equations describing the heat and mass transfer have to be analogous, but also the boundary conditions. They found that these boundary conditions could substantially differ in time and space.

Because moisture transport in the air and in the material is described by different potentials, conjugate drying models often use two solvers: one to solve the transport equations in the air and one to solve the transport in the porous material. When two solvers are used, a specific solution methodology is needed. Oliveira et al. [28] described such a solution procedure for laminar flow to study convective drying of a wood board and repeated the same procedure later to study soybean drying [33]. A finite element code was developed. In the first step the continuity and momentum equations in the air were solved separately. This is allowed if the flow is assumed steady and if the impact of density on the flow is neglected. The velocity field obtained from this calculation was assumed invariable during the rest of the simulation. Next the boundary layer was solved using boundary conditions of the first kind (constant temperature and concentration). The results of this numerical analysis were used to determine the heat and moisture fluxes at the surface. These fluxes were used as boundary conditions of the second kind for the porous material. Transport in the porous material was then solved. The temperature and moisture distribution in the porous material provided new boundary conditions for the air side for the next time step. This procedure was repeated until the final drying time is reached.

This explicit time marching procedure was also used by Murugesan et al. [34]. They developed a 2D finite element model to study the drying behaviour of ceramic brick. It was stated that buoyancy can have a significant effect on the transport mechanism in the air and must be taken into account by allowing changes of the flow field over time.

When explicit coupling procedures are used, two separate solvers can be used. This brings along the advantage that two separately developed models can be coupled and the developer of the drying model should only be concerned with the implementation of the coupling procedure. For example Gnoth et al. [35] developed a coupling procedure between a CFD model developed for cavities and a commercially available HAM model, Delphin® [22].

Defraeye et al. [11] coupled the commercial CFD package Fluent® with an in house developed HAM model HAMFEM [36]. When using an explicit coupling procedure, too large time steps will cause instability. Time steps should be small so that heat and mass fluxes at the material boundary do not change during a time step. Defraeye improved convergence by using an adaptive time stepping algorithm. This ensured that the optimal time step was used during the simulations. Nevertheless a long computational time was still needed even for relatively simple cases.

In literature, examples can be found where an implicit coupling is used for the heat and moisture transport equations. The unsteadiness that the explicit models are facing, is overcome and a significant reduction of computational time is noticed. De Bonis et al. [37] developed a finite element model using a commercial finite element package to study the performance of the drying process of fresh-cut vegetables. Lamnatou et al. [38, 39] developed a finite volume model to study the drying of apple slices.

Finally a hybrid approach is reported in literature. Saneinejad et al. [16] coupled a model for heat and mass transport with a commercial CFD model (Fluent®) and a radiation model to study the heat and moisture transport in a street canyon. Instead of calculating the fluxes at the air side and passing them to the material side explicitly, the transfer coefficients were calculated first at the air side. These transfer coefficients were then passed to the material side where they were implemented as an implicit boundary condition. This significantly improved convergence and solution stability.

### 3. Coupled heat and moisture model including vapour and liquid water transport

#### 3.1. Moisture transport in porous materials

Moisture in a building context can exist in three phases: vapour, liquid and solid (ice). In the present model ice and ice formation are neglected. The two remaining phases can both be stored and transported in a porous material. The moisture content in the porous material  $w$  is the sum of the vapour content  $w_v$  and the liquid content  $w_l$ . The vapour content is much smaller than the liquid content and is often neglected. The moisture flux in the material  $\vec{g}$  is the result of a vapour flux  $\vec{g}_v$  and liquid flux  $\vec{g}_l$ . This is of course only an approximation since both transport mechanisms can strictly speaking not be separated. Convection of air in the porous material is neglected. The vapour diffusion flux in a porous material can be described by an adjusted Fick's diffusion law.

$$\vec{g}_v = -\frac{\rho D_{va}}{\mu} \nabla Y = -\delta_v \nabla p_v \quad (1)$$

In this equation the total pressure is assumed constant, allowing the use of partial vapour pressure  $p_v$  instead of mass fraction  $Y$  as driving potential. For very small pores vapour diffusion can no longer be described by Fick's law. At these small scales collisions of vapour molecules and pore walls become more frequent than collisions between molecules. The vapour transport is then referred to as Knudsen diffusion or effusion. This Knudsen diffusion is also driven by vapour pressure gradients. To simplify the current model, the Knudsen diffusion is not modelled separately but its effect is assumed to be incorporated in the vapour diffusion resistance factor.

In these equations for diffusion the thermal diffusion or Soret effect is neglected. It was stated in Ref. [40] and shown by Whitaker [41] and Janssen [42] that this effect is small compared to the concentration diffusion.

The liquid flux is described by Darcy's law:

$$\vec{g}_l = -K_l \nabla p_c \quad (2)$$

The driving force for the liquid transport is the gradient in capillary pressure.. The moisture transport equation then results in:



$$\frac{\partial w}{\partial t} = \nabla \cdot (\vec{g}_v + \vec{g}_l) = \nabla \cdot \left( \frac{D_{va}}{\mu R_v T} \nabla p_v + K_l \nabla p_c \right) \quad (3)$$

It is now possible to transform this equation so that only two independent state variables remain. In this work temperature and capillary pressure are used in analogy to the work of Grunewald [43]. The partial vapour pressure is related to the relative humidity ( $RH = p_v/p_{vsat}$ ) and this relative humidity is in turn related to the capillary pressure by Kelvin's law (Eq. (4)).

$$p_c = \rho_l R_v T \ln RH \quad (4)$$

This results in the following equation for the moisture balance in a porous material:

$$\frac{\partial w}{\partial p_c} \frac{\partial p_c}{\partial t} = \nabla \cdot (K_l \nabla p_c) + \nabla \cdot \left( \frac{D_{va}}{\mu R_v T} \left( \frac{\rho_v}{\rho_l} \nabla p_c + \left( RH \frac{\partial p_{sat}}{\partial T} - \frac{p_v \ln RH}{T} \right) \nabla T \right) \right) \quad (5)$$

To solve Eq. (5) three material properties are needed: the vapour diffusion resistance factor  $\mu$ , the liquid permeability  $K_l$  and the moisture capacity  $\partial w/\partial p_c$ .

### 3.2. Heat transport in porous materials

Next the heat transport equations can be derived. Only transport by diffusion is assumed in the porous materials that are studied here. Heat is thus only transported in the porous materials due to conduction on the one hand and diffusion of moisture on the other hand. Water vapour diffusing through the porous material transports sensible as well as latent heat.

Conductive heat transport in a (porous) material can be described by Fourier's law for heat conduction:

$$\vec{q} = -\lambda_{mat} \nabla T \quad (6)$$

The conductivity of the porous material  $\lambda_{mat}$  is strongly dependent on the moisture content of the material since the conductivity of water differs from that of the material matrix.

Water is transported through a porous material as liquid and vapour resulting in a liquid and vapour flux. Along with the liquid water, sensible heat is transported while sensible and latent heat is transported along with the vapour diffusion.

The potential energy and kinetic energy changes in the porous material can be neglected and no chemical reactions occur in the material. The total energy of the porous material  $E$  is thus the sum of the energy stored in the material matrix and the energy stored in the liquid water and water vapour present in the material. The energy balance equation thus states that a change in stored energy is due to heat conduction and transport of latent and sensible heat along with the moisture transport:

$$\begin{aligned} \frac{\partial E}{\partial t} &= \frac{\partial}{\partial t} (\rho_{mat} h_{mat} + w_l h_l + w_v h_v) = \\ & (\rho_{mat} C_{mat} + w_l C_l + w_v C_v) \frac{\partial T}{\partial t} + C_l T \frac{\partial w_l}{\partial t} + (C_v T + L) \frac{\partial w_v}{\partial t} \\ &= \nabla \cdot (\lambda_{mat} \nabla T - C_l T \vec{g}_l - (C_v T + L) \vec{g}_v) \end{aligned} \quad (7)$$

$\rho_{mat}$  and  $C_{mat}$  are the dry porous material's density and heat capacity respectively. The liquid moisture content and vapour moisture content can be linked to the total moisture by the open porosity, taking into account that:

$$w = w_l + w_v \quad (8)$$

and

$$\psi_0 = \frac{w_l}{\rho_l} + \frac{w_v}{\rho_v} \quad (9)$$

### 3.3. Mass fraction or capillary pressure?

When only vapour diffusion is considered, the mass fraction of water vapour can be used as transport potential as for example proposed by Steeman et al. [9]. However using mass fraction as transport potential in a porous material when liquid transport is present, causes some difficulties as will be discussed in this section.

Transforming Darcy's law (Eq. (2)) for liquid transport from capillary pressure  $p_c$  to mass fraction  $Y$  results in:

$$\vec{g}_l = -K_l \nabla p_c = -K_l \frac{\partial p_c}{\partial RH} \frac{\partial RH}{\partial Y} \nabla Y - K_l \frac{\partial p_c}{\partial T} \nabla T \quad (10)$$

with

$$\frac{\partial p_c}{\partial RH} = \rho_l R_v \frac{T}{RH} \quad (11)$$

$$\frac{\partial p_c}{\partial T} = \rho_l R_v \ln RH + \rho_l R_v \frac{T}{RH} \frac{\partial RH}{\partial T} \quad (12)$$

It is thus mathematically possible to write Eq. (5) with mass fraction and temperature as the transported variables instead of capillary pressure and temperature. Difficulties in solving this model arise however when relative humidities near to 100% are encountered. This high relative humidity is typical when liquid moisture transport is present. Fig. 2 illustrates what happens when the mass fraction is near to the saturation mass fraction. This figure shows a psychrometric chart with the mass fraction on the vertical axis and the temperature on the horizontal axis. The figure starts from a state below the saturation line (situation ①). When the temperature is lowered, the mass fraction in the porous material is constant at first. The state of the porous material moves along a horizontal line from situation ① to situation ②. In situation ② the saturation mass fraction is reached. At temperature  $T_2$  the air in the porous material cannot hold more water vapour than  $Y_2$ . If the temperature would drop further to  $T_3$ , the mass fraction of water vapour in air is obliged to follow the saturation line. This implies that at saturation the mass fraction becomes temperature dependent. However for a good numerically solvable model, the transported variables should be independent.

As long as the relative humidity stays well below saturation, the state of the porous material can be described by the mass fraction  $Y$ . This is the case when only vapour transport is considered and when temperature changes are small. Steeman [9] confined his work to these conditions and was thus able to use mass fraction and temperature as transported variables for moisture and energy respectively.

Using mass fraction as transported variable is also allowed for isothermal liquid transport in porous materials. However, the assumption of isothermal conditions rarely holds. As an example the drying of a nearly saturated porous material is discussed.

A wet material that is nearly saturated will have a mass fraction of water vapour close to saturation and the relative humidity in the material will be almost 100%. During a convective drying process, water evaporates from the surface into the air flowing over the porous material. The amount of energy needed for this phase change (from liquid to vapour state) is the latent heat of evaporation. This energy is taken from the surrounding air and the porous material, thus resulting in a temperature drop of the material. When no other heat sources are present, the temperature of the porous material surface can drop to the wet bulb temperature. This temperature drop can be significant (e.g. air at 30°C and 40% RH has a wet bulb temperature of  $\pm 20^\circ\text{C}$ ). Since the mass fraction was already near saturation, a sudden drop in the temperature would mean that the mass fraction would also have to decrease. In other words the mass fraction becomes temperature dependent. The mass fraction

modelling approach proposed by Steeman [9] is thus no longer applicable for liquid transport phenomena such as convective drying.

From this discussion it is clear that the mass fraction cannot be used as the transported variable if liquid transport is included. Therefore the capillary pressure is proposed as the transported variable. The capillary pressure is not restricted by saturation conditions and is a better way to describe the state of a wet (nearly saturated) porous material.

### 3.4. Numerical implementation of the boundary conditions

As boundary conditions at the porous surfaces facing the air, heat and mass fluxes are imposed. These fluxes are calculated using Eqs. (13) and (14):

$$q = h^T (T_{ref} - T_s) \quad (13)$$

$$g = h_m^Y (Y_{ref} - Y_s) \quad (14)$$

$T_{ref}$  and  $Y_{ref}$  are reference values for temperature and mass fraction taken outside the boundary layer and  $T_s$  and  $Y_s$  are the temperature and mass fraction at the surface of the porous material.

The differential equations describing heat and moisture transport in the porous material are solved numerically together with the boundary conditions using a finite volume solver. Therefore the problem is discretized in time and space. To obtain a converged solution several iterations are needed within each time step. When the current iteration is indicated with superscript  $m$  and the next iteration is indicated with superscript  $m+1$ , the flux boundary conditions can be written as:

$$q^{m+1} = h^T (T_{ref} - T_s^{m+1}) \quad (15)$$

$$g^{m+1} = h_m^Y (Y_{ref} - Y_s^{m+1}) \quad (16)$$

This is the so-called implicit formulation. For the heat transport equation temperature is the transported variable which allows the direct implementation of Eq. (15). However the mass transport equations use capillary pressure as transported variable, thus Eq. (16) has to be reformulated to capillary pressure. The mass fraction at the boundary  $Y_s$  is a non-linear function of the capillary pressure. However Eq. (16) can be linearized around  $Y_s^m$ .

$$\begin{aligned} g^{m+1} &= h_m^Y (Y_{ref} - Y_s^{m+1}) \\ &= h_m^Y Y_{ref} - h_m^Y Y_s^{m+1} \\ &= h_m^Y Y_{ref} - h_m^Y \left[ \frac{p_{sat}}{\rho R_v T} \exp\left(\frac{p_c^{m+1}}{\rho_l R_v T}\right) \right] \\ &\approx h_m^Y Y_{ref} - h_m^Y \frac{p_{sat}}{\rho R_v T} \left[ \frac{1}{\rho_l R_v T} \exp\left(\frac{p_c^m}{\rho_l R_v T}\right) p_c^{m+1} + \exp\left(\frac{p_c^m}{\rho_l R_v T}\right) - \frac{1}{\rho_l R_v T} \exp\left(\frac{p_c^m}{\rho_l R_v T}\right) p_c^m \right] \end{aligned} \quad (17)$$

## 4. Experimental validation

The coupled heat and moisture model is validated by means of a convective drying experiment from literature [11]. In what follows, it will be shown that heat and mass transport cannot be solved separately when studying convective drying. At the same time drying rates are strongly determined by convective transport in the air.

In the first section, the experimental setup will be shortly described. Next, the simulation results of the coupled model are compared with the experimental data. Finally, neutron radiography measurements showing the moisture distribution in the brick sample were compared with the results of the coupled model.

#### 4.1. Experimental setup

Defraeye [11] constructed a small wind tunnel from transparent polymethyl methacrylate (PMMA) to perform convective drying experiments on building materials such as ceramic brick. A schematic representation of the wind tunnel with the test section is found in Fig. 3a. Air is drawn in by a fan, passes over a flow straightener (honeycomb) and flows through a convergent section before entering the test section. A detail of the test section is found in Fig. 3b.

The sample of ceramic brick measuring 10mm by 30mm by 90mm, was placed in a container of plexiglass (PMMA). The plexiglass had a thickness of 4mm. The sample of ceramic brick was wetted and placed in the wind tunnel in such a way that the top surface of the sample faces the air flowing through the tunnel. The sample was wetted to a moisture content of 126kg/m<sup>3</sup> which corresponds approximately to the capillary moisture content (130kg/m<sup>3</sup>). At the bottom of the container a layer of 20mm XPS insulation was installed. The front and back side of the container were covered with 15mm of XPS insulation, the side walls of the brick sample were insulated with 30mm of XPS. The sides of the sample were made impermeable for moisture. The open circuit wind tunnel was placed in a climate chamber where the mean temperature was set to 23.8°C (with a standard deviation of 0.2°C) and the mean relative humidity was set to 44% (with a standard deviation of 0.8%).

In the experiments, dry air flows over the top surface of the brick and the brick is dried out from one side, while the other sides are impermeable for moisture. During the drying experiment temperatures at the side of the ceramic brick were measured with thermocouples. Fig. 3a shows the location of these thermocouples. In total 6 thermocouples were installed at a side wall. The temperature was measured at a depth of 10mm, 20mm and 30mm from the material-air interface and 10mm in the lower insulation (at 40mm from the interface). To measure the inflow effect and the effect of a developing moisture and temperature boundary layer, a thermocouple was installed upstream and downstream of the centre thermocouples, both at a depth of 10mm. The accuracy of the thermocouples, as reported by Defraeye [11] was 0.1°C. The weight change of the test sample was continuously monitored by a balance. The balance was calibrated to an accuracy of 0.01g but in practice this accuracy was found to be 0.1g due to the impact of airflow on the balance. The velocity at the inlet of the test section and the turbulence intensity were measured with a PIV (particle image velocimetry) system. Defraeye [11] performed an extensive study on the accuracy of these PIV measurements. He concluded that a quantitative estimate of the uncertainty of the PIV measurements is difficult because of the presence of different sources of error in these measurement. Therefore best practice guidelines were followed. To obtain a reliable time-averaged mean air velocity, sufficient statistically independent double PIV images have to be taken. In his study 120 images at 2Hz were found to be sufficient. This led to an uncertainty of about 2% on the mean air velocity.

The test section can be assumed symmetric along the x-axis since the flow in the channel was found to be two-dimensional due to the high width to height ratio [44].

#### 4.2. Simulation model and settings

The experiments of Defraeye were used as a validation study for the newly developed coupled heat and moisture model. Preliminary simulations showed that 1D and 2D simulations were not sufficient to capture the heat and mass transport in the setup accurately and to incorporate phenomena such as the leading edge effect [10]. Therefore, a complex 3D simulation model of the brick was developed including the insulation and plexiglass out of which the sample container is built up.

Fig. 4 shows a 3D view of the test sample of ceramic brick embedded in the insulation and the plexiglass. The sample of ceramic brick measured 10mm thick by 30mm deep by 90mm long. Only half of the setup has been modelled due to symmetry, which considerably reduced the computational effort.

The inlet conditions of the air were measured by Defraeye [11]: the air inlet temperature was 23.8°C (with a standard deviation of 0.2°C) and the air inlet relative humidity was 44% (with a standard deviation of 0.8%). The temperature of the surroundings was constant and corresponded to the temperature of the climatic chamber (23.8°C).

The side faces facing the climate chamber (bottom, front, back and left face) of the setup were assumed impermeable for moisture. Moisture exchange is only possible at the top face. Heat can flow through all faces. At the side walls the heat flux is determined by Eq.(13), with  $T_s$  the temperature at the outer surface of the plexiglass and  $T_{ref}$  the temperature of the surroundings (i.e. 23.8°C). The heat transfer coefficient  $h$  is estimated at 8 W/m<sup>2</sup>K and incorporates both the effect of convection and radiation.

Due to the 2D airflow in the wind tunnel, the heat and mass transfer at the top face of the brick was assumed two-dimensional and varied along the length of the duct. The corresponding heat and mass transfer coefficients used for the simulations were determined by means of CFD simulations of the wind tunnel assuming a constant temperature at the bottom. Defraeye measured the velocity profile and turbulent intensity at the inlet of the test setup [11]. Fig. 5 shows these measured values for velocity and turbulent intensity. These measurements were used as input for the CFD simulation, together with the measured temperature and humidity.

The computational domain for the CFD simulation of the air flow was taken similar to that used by Defraeye [11] for his simulations. A 2D channel was simulated, corresponding to flow between two parallel plates. The channel had a height of 10mm as depicted in Fig. 3a. An inflow section of 15mm was taken and an outflow section of 30mm. These sections were adiabatic and impermeable for moisture. An appropriate grid was built consisting out of 4x10<sup>3</sup> quadrilateral control volumes. The grid was dense near the surfaces of the parallel plates and coarser to the centre. Steady Reynolds-averaged Navier-Stokes (RANS) was used in combination with a turbulence model. Here the realizable k-ε model was used with LRNM to take care of the viscosity affected region. Second order discretisation schemes were used. The SIMPLE algorithm was used for pressure-velocity coupling. Pressure interpolation was second order.

The mass transfer coefficient was determined through the heat and mass analogy. This analogy was shown to be valid by Defraeye [11] and by preliminary studies [10]. Especially during the constant drying rate period, when the temperature and moisture mass fraction at the surface are almost constant, this analogy applies. A power-law approximation of these coefficients as a function of the position in the duct is given by Eq. (18) a and b.

$$h^T(x) = 7.7577x^{-0.2959} \quad (18a)$$

$$h_m^Y(x) = \rho R_v T 5.514 \cdot 10^{-9} x^{-0.2959} \quad (18b)$$

Radiation at the brick-air interface was taken into account in a simplified way by assuming that the brick top surface only sees the upper wall of the wind tunnel, which results in a view factor of 1. The temperature of the top wall of the wind tunnel was measured. An average value of 23.3°C was found. The radiant heat flux at the brick-air interface can be calculated as:

$$q_{rad} = \frac{C_b}{\frac{1}{\varepsilon_1} + \frac{1}{\varepsilon_2} - 1} (T_{roof}^4 - T_s^4) \quad (19)$$

With  $q_{rad}$  (W/m<sup>2</sup>) the radiant heat flux between the roof of the wind tunnel and the brick surface,  $T_{roof}$  the temperature at the top wall of the wind tunnel,  $T_s$  the surface temperature of the brick and  $\varepsilon_1$  and  $\varepsilon_2$  the emissivity of the roof and the brick surface, which are assumed to be 0.97 and 0.93 respectively.

For these simulations a grid sizing 114x93x35 was used (371070 cells). The grid was denser near the top. A grid independency test was carried out by performing a simulation with a denser grid. This simulation showed no significant difference with the original grid. Therefore, the original grid of

114x93x35 was retained for the current simulations. For these transient simulations a time step of 60 seconds was taken. In total a drying period of 12 hours was simulated, resulting in a total of 720 time steps.

The material properties of ceramic brick that have been used in the simulations are shown in Table 1. They have been determined experimentally by Ref. [45]. The vapour diffusion coefficient  $\delta_v$  was approximated by Eq. (20) and the moisture retention curve  $w(p_c)$  was formulated by Eq. (21) [45]:

$$\delta_v = \frac{2.61 \times 10^{-5}}{\mu_{dry} R_v T} \frac{1 - \left(\frac{w}{w_{cap}}\right)}{0.503 \left(1 - \left(\frac{w}{w_{cap}}\right)\right)^2 + 0.497} \quad (20)$$

$$w(p_c) = w_{cap} [0.846(1 + (1.394 \times 10^{-5} p_c)^4)^{-0.75} + 0.154(1 + (0.9011 \times 10^{-5} p_c)^{1.69})^{-0.408}] \quad (21)$$

The liquid permeability  $K_l$  is given by Eq. (22) [45]. The corresponding coefficients are listed in Table 2.

$$K_l = K_s \left[ \sum_{i=1}^3 w_i (1 + (-\alpha_i p_c)^{-n_i})^{-m_i} \right]^{\tau} \times \left( \frac{\sum_{i=1}^3 \alpha_i w_i \left( 1 - \frac{(-\alpha_i p_c)^{n_i}}{1 + (-\alpha_i p_c)^{n_i}} \right)^{m_i}}{\sum_{i=1}^3 \alpha_i w_i} \right) \quad (22)$$

### 4.3. Comparison between simulations and experiments

#### *Temperature change and scaled mass loss*

Temperatures measured at depths of 10mm, 20mm, 30mm (at the interface brick/insulation) and 40mm (10mm in the insulation) are compared with the simulations. Fig. 6 compares the measured temperatures with the simulations. The dashed line shows the simulation outcome using the original material properties as reported in Table 1 and Eqs. (20)-(22). The red and green lines in Fig. 6 are explained in Section 4.4. A measurement uncertainty of 0.1°C was reported [11] and is indicated in Fig. 6.

Overall a good agreement between the model and the experiments is found. The largest deviations are found near the surface. The temperature at a depth of 10mm is slightly underestimated by the model (0.3-0.4°C). Also the onset of the FRP (when the temperature starts to rise again) is delayed in the simulations (see Fig. 6(a)-(c)). This leads to a temperature mismatch of up to 1°C between measured and predicted temperatures. Nevertheless, the equilibrium temperature (the lowest temperatures in Fig. 6) is closely approximated by the model (within the error bars). Deeper in the material, the approximation becomes even better. At a depth of 40mm (10mm in the insulation), the agreement is almost perfect (within the error bars). This indicates that the applied boundary conditions closely approach reality.

Fig. 7 compares the measurements and simulation results of the temperatures along the length of the sample at a depth of 10mm in the sample. Although there is no perfect match between simulations and experiments the trends are well predicted: the upstream temperature reaches the same equilibrium temperature as the centre temperature both in the simulations and the measurements. However dry-out occurs sooner upstream which results in a faster occurring temperature rise upstream. Downstream the temperature is higher both in the measurements and in the simulations. The onset of dry-out happens later here and this delays the temperature rise.

During the experiments, the weight change of the sample was also monitored (Fig. 8). The mass loss was scaled using the initial moisture content of the brick sample: i.e. 3.4g. Due to this small initial

moisture content and relative high weight of the sample and test section itself (i.e.  $\pm 827$  g), the weight change was difficult to measure. An uncertainty of 0.1g on the weight measurement was reported [11], the uncertainty on the weight change was 0.14g. This resulted in an uncertainty of 4% on the scaled mass loss.

The experiments clearly show a constant slope in the mass loss curve for the first three hours (Figure 8). During this initial drying rate period (CRP) the moisture content in the brick decreases linearly. A similar duration was found in the simulations. Next, the FRP starts: this is shown by a decreasing slope of the mass loss curve in Fig. 8. Comparison of the measurements and the simulations shows that the mass loss during the CRP is well-predicted but that there is an overestimation of the mass loss during the FRP.

#### *Moisture distribution profiles*

It is clear from the previous analysis that the model is able to predict the correct trends but that there is still a significant deviation between the measured and predicted mass loss. To explain the cause for this deviation, measurement data are needed of the moisture distribution inside the brick. Data provided by the Swiss Federal Laboratories for Materials Science and Technology (EMPA) was therefore used to further study the moisture transport in the ceramic brick. With neutron radiography this research group was able to measure the moisture content evolution in the ceramic brick over the depth of the sample. More details on the used measurement setup can be found in Refs. [46-48].

Fig. 9a shows the comparison of the moisture content distribution in the ceramic brick over time for the simulation and the measurements. This comparison shows that during the first hours the agreement is fairly good, but at later times (after 3 hours) the simulation shows a faster decrease of the moisture content compared to the measurements. This is in agreement with the mass measurements and simulation shown in Fig. 8, which showed a good agreement during the CRP (first 3 hours) and afterwards an overestimation of the simulated mass loss.

It should be noted that for a correct comparison between the measured and the modelled moisture content only the central region in the brick, between 0.5cm and 2.5cm, should be compared. This is due to some scattering that was present in the neutron radiography measurements. This resulted in a falsely decreasing moisture content at the bottom of the sample and a too fast decreasing moisture content at the top.

#### **4.4. Influence of material properties**

Material properties have a large impact on these simulations. Correct material properties play a major role in the validation process, since uncertainty on material properties can be large and the consequences correspondingly. Previous studies have already shown that the hygric material properties, namely retention curve, permeability and water vapour resistance diffusion factor are the most important [11,49,50]. Fig. 8 shows a systematic overestimation of the mass loss in the brick, which raises the suspicion that the deviation is caused by uncertainties in the material properties. Defraeye did not list uncertainties on the measured material properties that he provided in his study [11], but he performed a similar study [50] on ceramic brick. In this paper standard deviations on the measured material properties were listed. Table 3 lists these standard deviations as reported by Defraeye [50].

The comparison of measurements and simulations in Figs.6 and 8 showed that the first drying period is well captured. This suggests that the permeability and the retention curve at high moisture contents agree well with reality. The large deviations occur during the second drying rate period.

To investigate the effect of the material properties on the modelling outcome, the main parameters (permeability, retention curve and water vapour resistance diffusion factor) were examined closer. First of all it was found that increasing the water vapour resistance diffusion factor from 24.79 to 32 had no significant impact on the mass loss in the brick and on the moisture distribution.

Next the vapour retention curve was adjusted in such a way that the curve only changed at high capillary pressures, so it would not affect the drying behaviour during the first drying period. Fig. 10 shows the original retention curve as found by Ref. [45] and the adjusted curve. The adjusted moisture retention curve can be formulated by Eq. (23).

$$w(p_c) = w_{cap} [0.5(1 + (1.394 \times 10^{-5} p_c)^4)^{-0.75} + 0.5(1 + (0.9011 \times 10^{-5} p_c)^{1.69})^{-0.408}] \quad (23)$$

Fig. 9b shows the simulation results of the moisture distribution for the adjusted moisture retention curve. When comparing Fig. 9b with Fig. 9a, a better agreement is shown when the retention curve is adjusted. However, the agreement only improves for the overall moisture content in the brick. The distribution of the moisture content deviates from the one measured by neutron radiography. For the altered retention curve the drying front moves too fast into the brick compared to the measurements. Adjusting the retention curve thus improves the overall moisture content prediction, as also shown in Fig. 8, but does not improve the moisture content distribution. This suggests that deviations between measurements and simulations with the original material data cannot solely be caused by uncertainties in the estimated retention curve.

To further study this, the liquid permeability was also altered. The original retention curve [45] and the adjusted curve are shown in Fig. 11. The adjusted liquid permeability can be approximated with Eq. (22) and by using “ $w_i$  adjusted” instead of “ $w_i$ ” as listed in Table 2.

By lowering the permeability, a better agreement can be found between measurements and simulations as shown in Fig. 9c. The agreement is also better for the overall moisture content (Fig. 8). Although uncertainty exists on all material parameters, in this case it is most likely that the largest deviations are caused by the uncertainty on the liquid permeability.

Of course some deviations between the measurements and the simulations can still be observed after the material properties are adjusted. This can be mainly attributed to uncertainties in the implemented boundary and initial conditions.

During the simulations, the heat transfer coefficient at the side walls was estimated and the inlet temperature was assumed to be constant, though in reality the temperature varied slightly. Also an uncertainty of 2% on the inlet velocity profile that was measured using PIV, was found [11].

Finally it can be stated that some of the deviations are caused by uncertainty in the numerical modelling, but this is rather difficult to quantify. Only an improvement of the modelling techniques can overcome or reduce this uncertainty. Possible uncertainties arising from the numerical model are:

- Errors caused by discretisation
- Errors caused by simplifications in the model (simplified radiation modelling, assuming perfect straight and aligned surfaces, assuming constant transfer coefficients at some surfaces...)

Of course, a model is always a simplification of reality. The art of modelling is to apply the correct choices for simplifications so that the simulation result is acceptably close to reality.

#### 4.5. Discussion

Fig. 8 compares the mass loss computed with the original material data and the mass loss computed with the adjusted retention curve and liquid permeability. Both changes agree well with the mass loss measurements. But, as shown in Fig. 9, a good prediction of the mass loss does not imply a good prediction of the moisture content distribution. It can thus be stated that both mass loss and moisture distribution predictions should be validated before a conclusion can be drawn on the correctness of the model and the used material properties.

Nevertheless, a good agreement for moisture does not guarantee a good agreement for temperature as is seen in Fig. 6. Since heat and moisture transport in porous materials are strongly coupled, changes in retention curve or liquid permeability have consequences for both temperature and moisture distribution. Where before the model underestimated the temperature, the model now seems to overestimate the temperature both for the adjusted retention curve and the adjusted liquid permeability. Since the model with the adjusted retention curve and the model with the adjusted



permeability result in similar mass loss curves (Fig. 8), the drying rates for both cases will be similar. And since the temperature in the brick is to a great extent determined by the drying rate due to the latent heat loss, the predicted temperature curves are similar for both cases.

The original model thus underpredicts the temperature whereas the adjusted models overpredict the temperature. However, the magnitude of difference between measurements and simulations for the original case and the altered cases is similar. The model with an adjusted retention curve and the model with an adjusted permeability do not result in a worse agreement of temperature, but at the same time there is also no improvement. It is thus difficult to make a sound conclusion on the impact that the adjustments have on the temperature course in the material.

## 5. Conclusion

In this paper a newly developed coupled heat and moisture model including vapour and liquid moisture transport was presented. The model enables to describe the coupled heat and mass transfer in porous building materials. Contrary to some heat and moisture models that only include vapour transport, the newly developed model has a broader application range, as it can be used to study vapour diffusion through porous materials and capillary moisture transport. The model lends itself to study the drying phenomena of porous materials.

In this paper the new model was described and validated against a drying experiment from literature, in which ceramic brick is used as a porous material. The validation study showed that the experimental results agreed well with the simulations results of a 3D model. Nevertheless, some deviations could be noted which were attributed to uncertainty of the material properties, especially of the liquid permeability and retention curve. By altering the liquid permeability or retention curve, the agreement between simulations and measurements improved.

Comparison with neutron radiography measurements revealed that a good agreement of the overall moisture content does not guarantee a good agreement of the moisture distribution in the porous material. The moisture distribution measurements showed that the best agreement was found for an adjusted liquid permeability. Adjusting the sorption isotherm resulted in a drying front moving too fast into the porous material.

## Acknowledgements

The results presented in this paper were obtained within the frame the research project IWT-SB/81322/Van Belleghem funded by the Flemish Institute for the Promotion and Innovation by Science and Technology in Flanders and IWT SBO-050451 project Heat, Air and Moisture Performance Engineering: A Whole Building Approach. Their financial support is gratefully acknowledged.

Special thanks go to Prof. Dominique Derome and Dr. Peter Moonen from EMPA Zurich and to Dr. Thijs Defraeye from KULeuven for their willingness to provide some of the necessary measurement data.

## References

- [1] L. Fang, G. Clausen, P.O. Fanger. Impact of temperature and humidity on the perception of indoor air quality. *Indoor Air*, 8:80-90, 1998.
- [2] C. J. Simonson, M. Salonvaara, T. Ojanen. The effects of structures on indoor humidity e possibility to improve comfort and perceived air quality. *Indoor Air*, 12:243-51, 2002.
- [3] N. Mendes, F.C. Winkelmann, R. Lamberts and P.C. Philippi. Moisture effects on conduction loads. *Energy and Buildings*, 35(7):631–644, 2003.
- [4] O.F.Osanyintola and C.J. Simonson. Moisture buffering capacity of hygroscopic building materials: experimental facilities and energy impact. *Energy and Buildings*, 38(10):1270-82, 2006.
- [5] E. Vereecken and S. Roels. Review of mould prediction models and their influence on mould risk evaluation. *Building and Environment*, 51(0):296-310, 2012.
- [6] M. Woloszyn and C. Rode. IEA ANNEX41 Whole Building Heat, Air and Moisture Response - Subtask1: Modelling Principles and Common Exercises. Technical report, 2008.

- [7] M. Steeman, A. Janssens, H.-J. Steeman, M. Van Belleghem, M. De Paepe. On coupling 1D non-isothermal heat and mass transfer in porous materials with a multizone building energy simulation model. *Building and Environment*, 45:865-77, 2010
- [8] M. Steeman, M. Van Belleghem, M. De Paepe and A. Janssens. Experimental validation and sensitivity analysis of a coupled BES-HAM model. *Building and Environment*, 45(10):2202-2217, 2010.
- [9] H.-J. Steeman, M. Van Belleghem, A. Janssens, M. De Paepe. Coupled simulation of heat and moisture transport in air and porous materials for the assessment of moisture related damage. *Building and Environment*, 44(10):2176-84, 2009.
- [10] M. Van Belleghem. Modelling coupled heat and moisture transfer between air and porous materials for building applications. PhD thesis. Ghent University, Belgium, 2013.
- [11] T. Defraeye. Convective Heat and Mass Transfer at Exterior Building Surfaces. PhD thesis, KULeuven, Belgium, 2011.
- [12] M. Van Belleghem, M. Steeman, A. Willockx, A. Janssens and M. De Paepe. Benchmark experiments for moisture transfer modelling in air and porous materials. *Building and Environment*, 46(4):884-898, 2011.
- [13] L. H.Mortensen, M. Woloszyn, C. Rode and R. Peuhkuri. Investigation of microclimate by CFD modeling of moisture interactions between air and constructions. *Journal of Building Physics*, 30(4):279–315, 2007.
- [14] T. Defraeye, B. Blocken, and J. Carmeliet. Analysis of convective heat and mass transfer coefficients for convective drying of a porous flat plate by conjugate modelling. *International Journal of Heat and Mass Transfer*, 55(1-3):112–124, 2012.
- [15] T. Defraeye, G. Houvenaghel, J. Carmeliet and D. Derome. Numerical analysis of convective drying of gypsum boards. *International Journal Heat and Mass Transfer* 55(9-10): 2590-2600, 2012.
- [16] S. Saneinejad, P. Moonen, T. Defraeye, D. Derome and J. Carmeliet. Coupled CFD, radiation and porous media transport model for evaluating evaporative cooling in an urban environment. *Journal of Wind Engineering and Industrial Aerodynamics*, 104(0): 455-463, 2012.
- [17] M. Van Belleghem, M. Steeman, A. Janssens and M. De Paepe. Heat, air and moisture transport modelling in ventilated cavity walls. Submitted to *Journal of Building Physics*. 2013.
- [18] P. C. D. Milly. Moisture and heat transport in hysteretic, in homogeneous porous media: a matrix head-based formulation and a numerical model. *Water Resources Research—Water Resources Research*, 18(3):489–98, 1982.
- [19] K. Abahri, R. Belarbi and A. Trabelsi. Contribution to analytical and numerical study of combined heat and moisture transfers in porous building materials. *Building and Environment*, 46(7):1354–1360, 2011.
- [20] K. A. Landman, L. Pel and E.F. Kaasschieter. Analytic modelling of drying of porous materials. *Mathematical Engineering in Industry*, 8(2):89–122, 2001.
- [21] D. Zirkelbach, T. Schmidt, H. M. Künzel, M. Kehrer and C. Bludau. WUFI 2D, 2007.
- [22] Bauklimatik Dresden. Delphin. <http://bauklimatik-dresden.de/delphin/index.php>.
- [23] D. Berger and D. C. T. Pei. Drying of hygroscopic capillary porous solids - a theoretical approach. *International Journal of Heat and Mass Transfer*, 16:293–302, 1973.
- [24] W. Masmoudi and M. Prat. Heat and Mass-Transfer between a Porous- Medium and a Parallel External Flow - Application to Drying of Capillary Porous Materials. *International Journal of Heat and Mass Transfer*, 34(8):1975–1989, 1991.
- [25] V.P.C. Mohan and P. Talukdar. Three dimensional numerical modeling of simultaneous heat and moisture transfer in a moist object subjected to convective drying. *International Journal of Heat and Mass Transfer*, 53(21-22):4638–4650, 2010.
- [26] H. Shokouhmand, V. Abdollahi, S. Hosseini and K. Vahidkhah. Performance Optimization of a Brick Dryer Using Porous Simulation Approach. *Drying Technology*, 29(3):360–370, 2011.
- [27] A. Kaya, O. Aydin and I. Dincer. Numerical modeling of heat and mass transfer during forced convection drying of rectangular moist objects. *International Journal of Heat and Mass Transfer*, 49(17-18):3094–3103, 2006.
- [28] L. S. Oliveira and K. Haghghi. Conjugate heat and mass transfer in convective drying of porous media. *Numerical Heat Transfer, Part A: Applications*, 34(2):105–117, 1998.
- [29] T. Defraeye, B. Blocken, D. Derome, B. Nicolai and J. Carmeliet. Convective heat and mass transfer modelling at air–porous material interfaces: Overview of existing methods and relevance. *Chemical Engineering Science* 74:49-58, 2012
- [30] H. Amir, G.Le Palec and M. Daguene. S'échage superficiel d'un matériau poreux humide par convection forcée d'air chaud: couplage entre les équations de transfert dans le matériau et celles de la couche limite. *International Journal of Heat and Mass Transfer*, 30(6):1149–1158, 1987.

- [31] B. Zeghmati, M. Daguene, and G. Le Palec. Study of transient laminar free convection over an inclined wet flat plate. *International Journal of Heat and Mass Transfer*, 34(4/5):899–909, 1991.
- [32] A. A. Dolinskiy, A. S. H. Dorfman, and B. V. Davydenko. Conjugate heat and mass transfer in continuous processes of convective drying. *International Journal of Heat and Mass Transfer*, 34(11):2883–2889, 1991.
- [33] L. S. Oliveira and K. Haghghi. Conjugate Heat and Mass Transport in Convective Drying of Multiparticle Systems Part II: Soybean Drying. *Drying Technology*, 16(3-5):463–483, 1998.
- [34] K. Murugesan, H. N. Suresh, K. N. Seetharamu, P. A. A. Narayana, and T. Sundararajan. A theoretical model of brick drying as a conjugate problem. *International Journal of Heat and Mass Transfer*, 44(21):4075–4086, 2001.
- [35] S. Gnath, F. Hansel, P. Hupl, and H. Fechner. Aero-hygrothermisches Verhalten von Umfassungskonstruktionen mit Hohlrumen. *Bauphysik*, 30(6):380–388, 2008.
- [36] H. Janssen, B. Blocken, and J. Carmeliet. Conservative modelling of the moisture and heat transfer in building components under atmospheric excitation. *International Journal of Heat and Mass Transfer*, 50(5-6):1128–1140, 2007.
- [37] M. V. De Bonis and G. Ruocco. A generalized conjugate model for forced convection drying based on an evaporative kinetics. *Journal of Food Engineering*, 89(2):232–240, 2008.
- [38] C. Lamnatou, E. Papanicolaou, V. Belessiotis, and N. Kyriakis. Finitevolume modelling of heat and mass transfer during convective drying of porous bodies - Non-conjugate and conjugate formulations involving the aerodynamic effects. *Renewable Energy*, 35(7):1391–1402, 2010.
- [39] C. Lamnatou, E. Papanicolaou, V. Belessiotis, and N. Kyriakis. Numerical study of the interaction among a pair of blunt plates subject to convective drying - A conjugate approach. *International Journal of Thermal Sciences*, 49(12):2467–2482, 2010.
- [40] K.M. Waananen, J.B. Litchfield and M.R. Okos. 1993, Classification of drying models for porous solids. *Drying Technology*, 11(1):1-40, 1993.
- [41] S. Whitaker. The role of irreversible thermodynamics and the Onsager relations in the analysis of drying phenomena. *Proc. sixth International Drying Symposium IDS'88*, 1988.
- [42] H. Janssen 2011. Thermal diffusion of water vapour in porous materials: Fact or fiction? *International Journal of Heat and Mass Transfer*, 54(7-8):1548-1562, 2011.
- [43] J. Grunewald. Diffusiver und konvektiver Stoff- und Energietransport in kapillarporösen Baustoffen. PhD. Technische Universität Dresden, 1997.
- [44] R. B. Dean. Reynolds Number Dependence of Skin Friction and Other Bulk Flow Variables in Two-Dimensional Rectangular Duct Flow. *Journal of Fluids Engineering*, 100(2):215–223, 1978.
- [45] H. Derluyn, H. Janssen, P. Moonen and J. Carmeliet. moisture transfer across the interface between brick and mortar joint. *Proceedings of the 8<sup>th</sup> Symposium on Building Physics in Nordic Countries (NSB2008)*, Copenhagen, June 16-18, 2008.
- [46] H. Derluyn, M. Griffa, D. Mannes, I. Jerjen, J. Dewanckele, P. Vontobel, A. Sheppard, M. N. Boone, D. Derome, E. H. Lehmann and J. Carmeliet. Probing salt crystallization damage mechanisms in porous limestone with neutron radiography and X-ray tomography. In *5th International Building Physics Conference (IBPC2012)*, Kyoto, Japan, 2012.
- [47] M. Sedighi-Gilani, M. Griffa, D. Mannes, E. Lehmann, J. Carmeliet and D. Derome. Visualization and quantification of liquid water transport in softwood by means of neutron radiography. *International Journal of Heat and Mass Transfer*, 55(21-22):6211–6221, 2012.
- [48] E.H. Lehmann, G. Frei, G. Khne and P. Boillat. The micro-setup for neutron imaging: A major step forward to improve the spatial resolution. *Nuclear Instruments and Methods in Physics Research Section A: Accelerators, Spectrometers, Detectors and Associated Equipment*, 576(23):389–396, 2007.
- [49] M. Van Belleghem, H.-J. Steeman, M. Steeman, A. Janssens and M. De Paepe. Sensitivity analysis of CFD coupled non-isothermal heat and moisture modelling. *Building and Environment*, 45(11):2485-2496, 2010.
- [50] T. Defraeye, B. Blocken and J. Carmeliet. Influence of uncertainty in heat-moisture transport properties on convective drying of porous materials by numerical modelling. *Chemical Engineering Research and Design*, 91:36-42, 2013
- [51] Mujumdar AS. *Handbook of industrial drying*. 3th ed. CRC Press; 2007.

## List of Figures

Fig. 1. Typical surface averaged drying rate (the dashed line indicates the drying rate in case the initial temperature is higher or lower than the wet bulb temperature), based on [51].

Fig. 2. Psychrometric chart, saturation mass fraction indicated in blue.

Fig. 3. Schematic representation of wind tunnel and test section used to perform drying experiments. Based on [11].

- (a) Wind tunnel side view and top view
- (b) Model of test section of experimental setup

Fig. 4. 3D simulation model of the test sample.

Fig. 5. Velocity profile (m/s) and turbulent intensity (-) as measured by Defraeye [11].

Fig. 6. Comparison between heat and moisture transport model with original material data (- -), model with adjusted retention curve (- - -) and model with adjusted liquid permeability (- - -). Temperature measurement indicated by (\*).

- (a) Temperature at 10mm in the brick
- (b) Temperature at 20mm in the brick
- (c) Temperature at 30mm, at bottom of brick
- (d) Temperature at 40mm, 10mm in insulation

Fig. 7. Simulated temperature in the ceramic brick, upstream of the centre (blue), in the centre (black) and downstream (red). Comparison with measurements upstream (o), centre (□) and downstream (▲).

Fig. 8. Scaled mass loss. Comparison of experiment (■), CFD-HAM simulation with original material properties (- -) , with adjusted retention curve (- -) and adjusted liquid permeability (- -).

Fig. 9. Comparison of the measured (- -) and simulated (- -) moisture content distribution in the ceramic brick sample over time. Time difference between two lines is 1 h.

- (a) Moisture distribution when using the original material properties as reported by [46]
- (b) Moisture distribution when using an adjusted retention curve
- (c) Moisture distribution when using an adjusted liquid permeability

Fig. 10. Retention curve of brick: original curve [45] (- -) and adjusted curve (- - -).

Fig. 11. Liquid permeability of ceramic brick: original curve [45] (- -) and adjusted curve (- - -).

## List of Tables

Table 1. Material properties of ceramic brick [45].

Table 2. Parameters in Eq. (22) [45].

Table 3 Standard deviations of material properties as listed by Ref. [50].

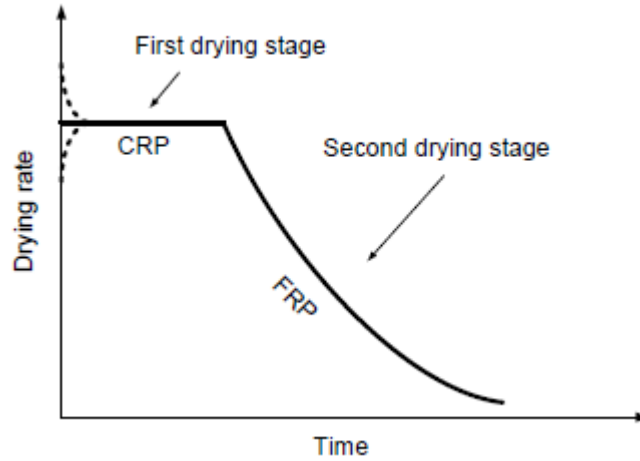


Fig. 1. Typical surface averaged drying rate (the dashed line indicates the drying rate in case the initial temperature is higher or lower than the wet bulb temperature), based on [51].

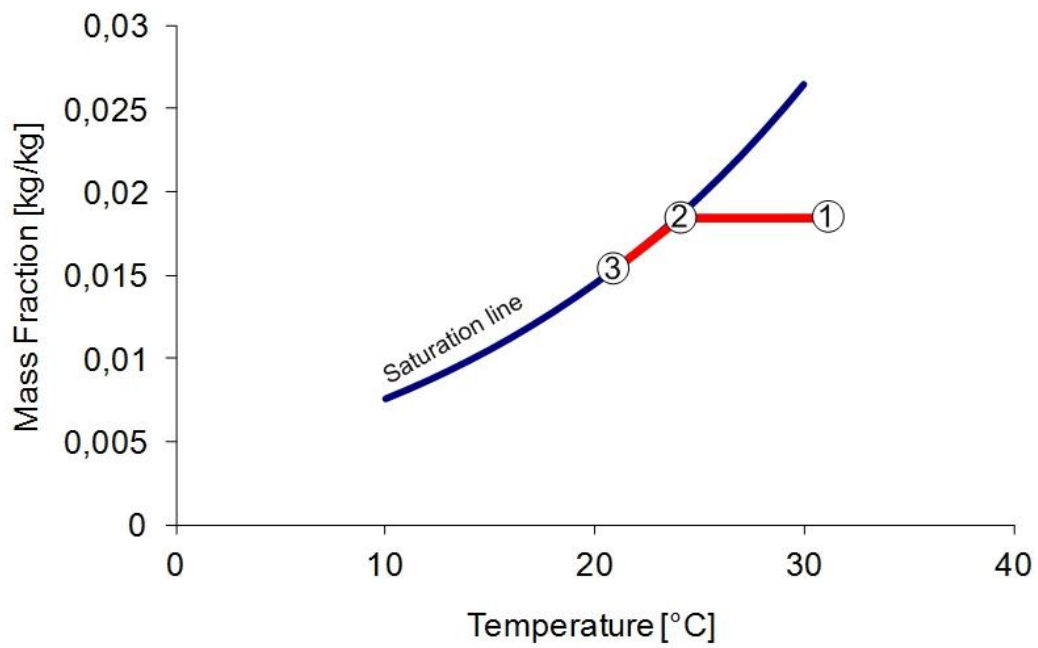
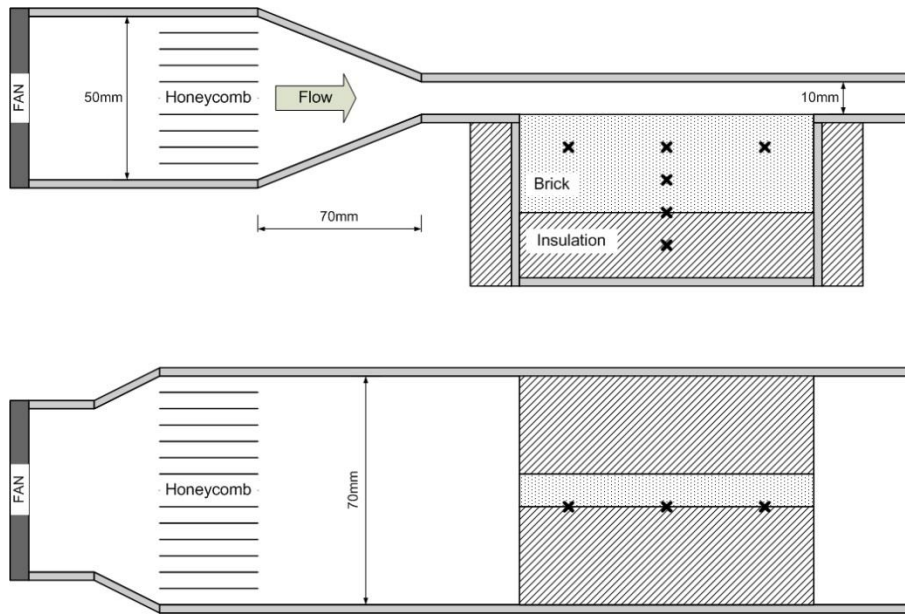
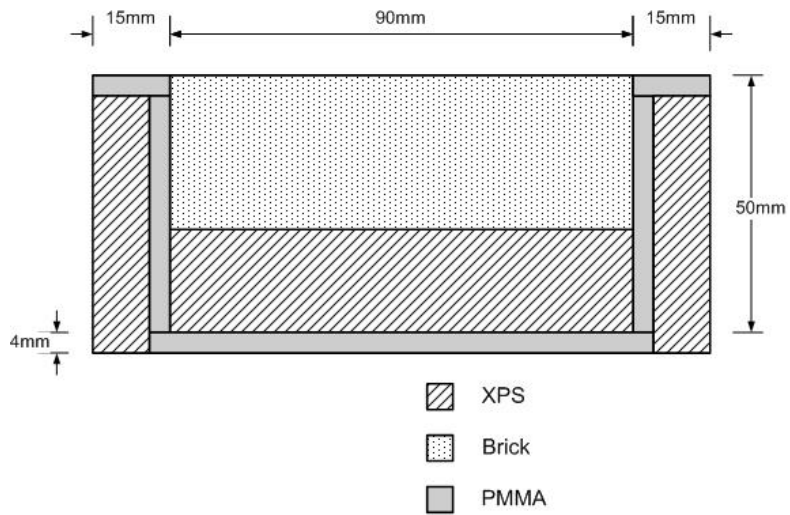





Fig. 2. Psychrometric chart, saturation mass fraction indicated in blue.



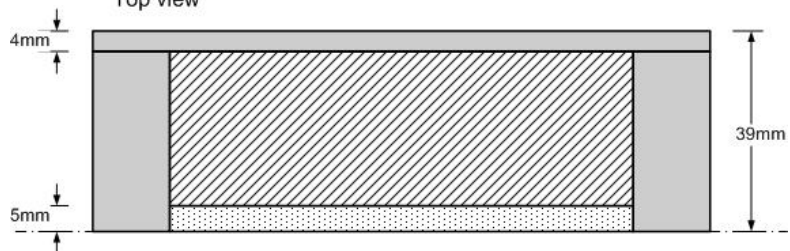
(a) Wind tunnel side view and top view

Vertical cross section



-  XPS
-  Brick
-  PMMA

Top view



(b) model of test section of experimental setup

Fig. 3. Schematic representation of wind tunnel and test section used to perform drying experiments. Based on [11].

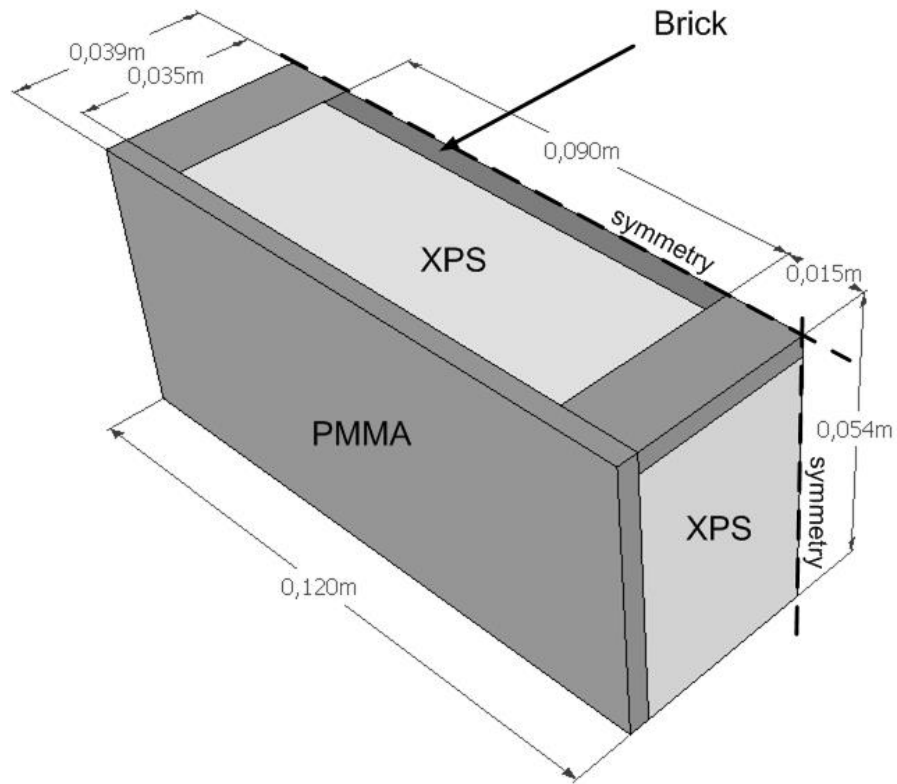


Fig. 4. Schematic representation of the 3D simulation model of the test sample.

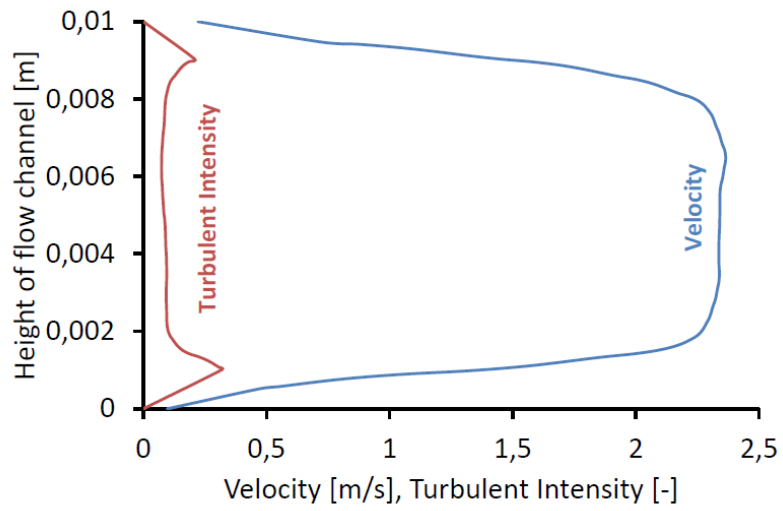
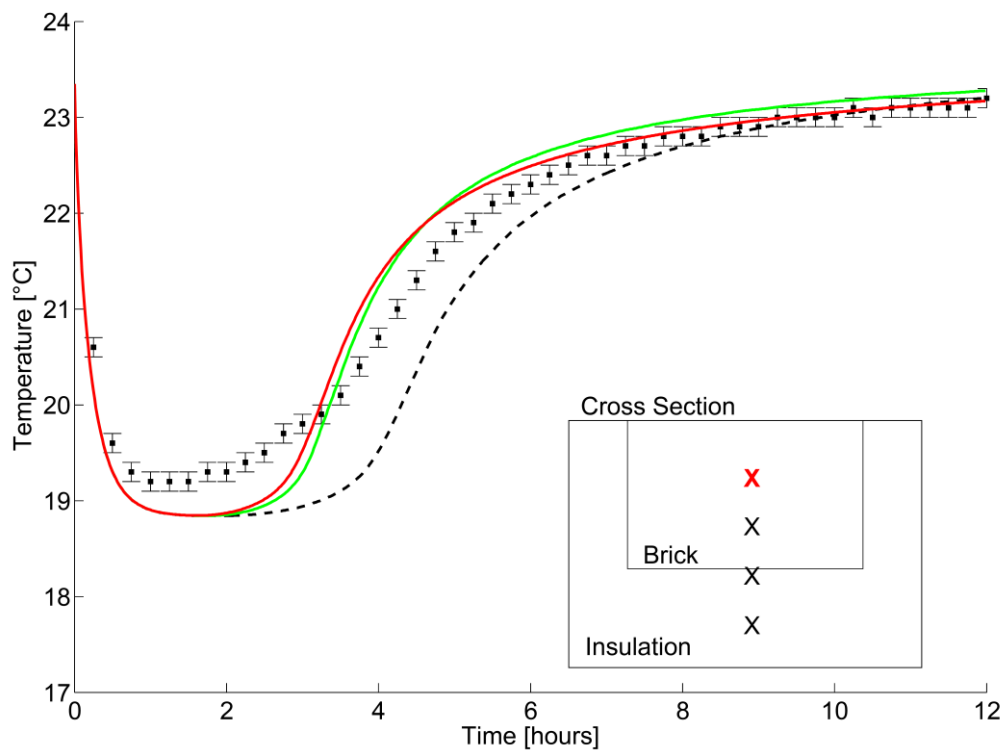
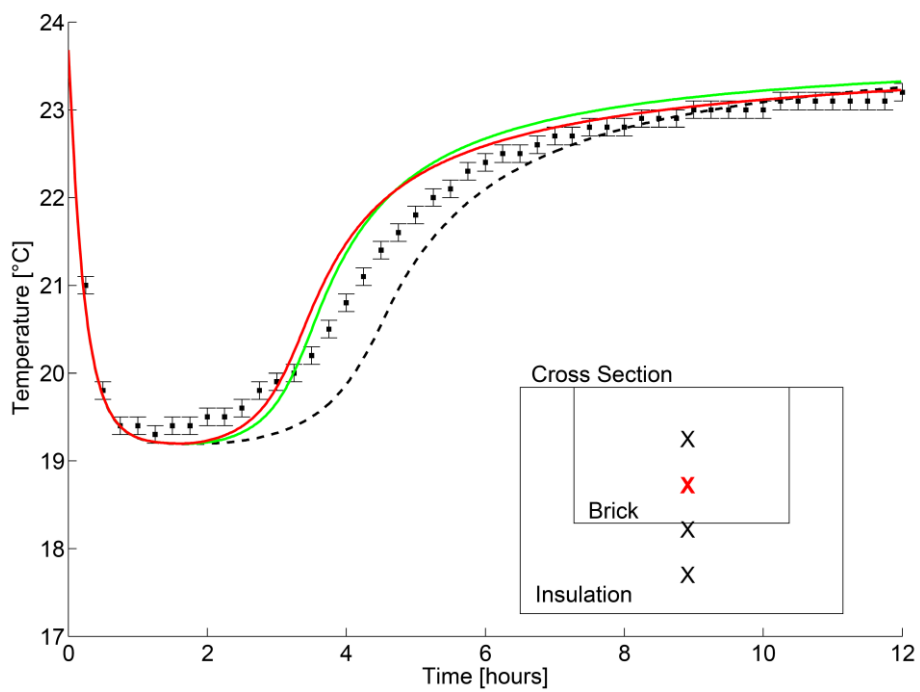


Fig. 5. Velocity profile (m/s) and turbulent intensity (-) as measured by Defraeye [11].

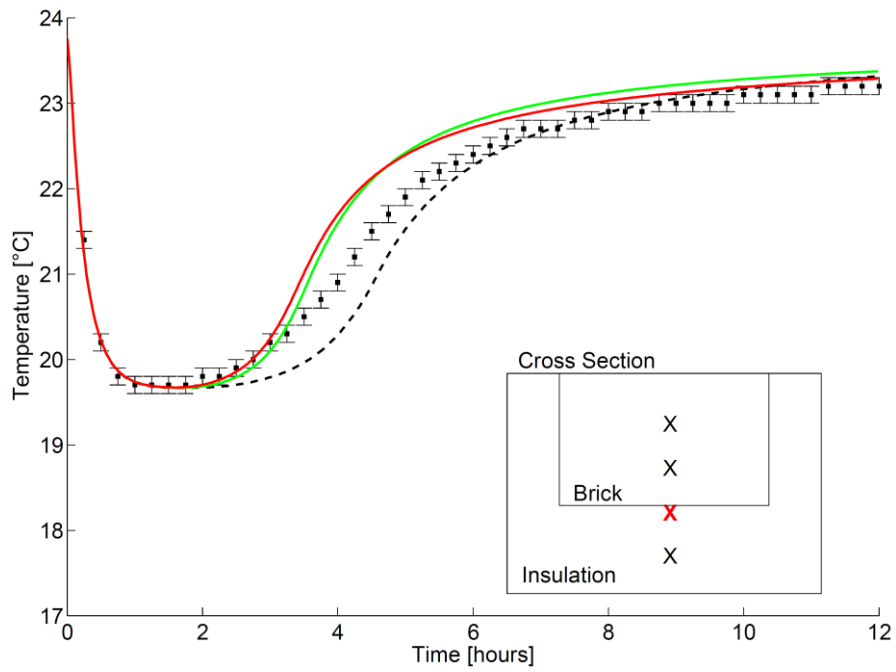


(a) Temperature at 10mm, in brick

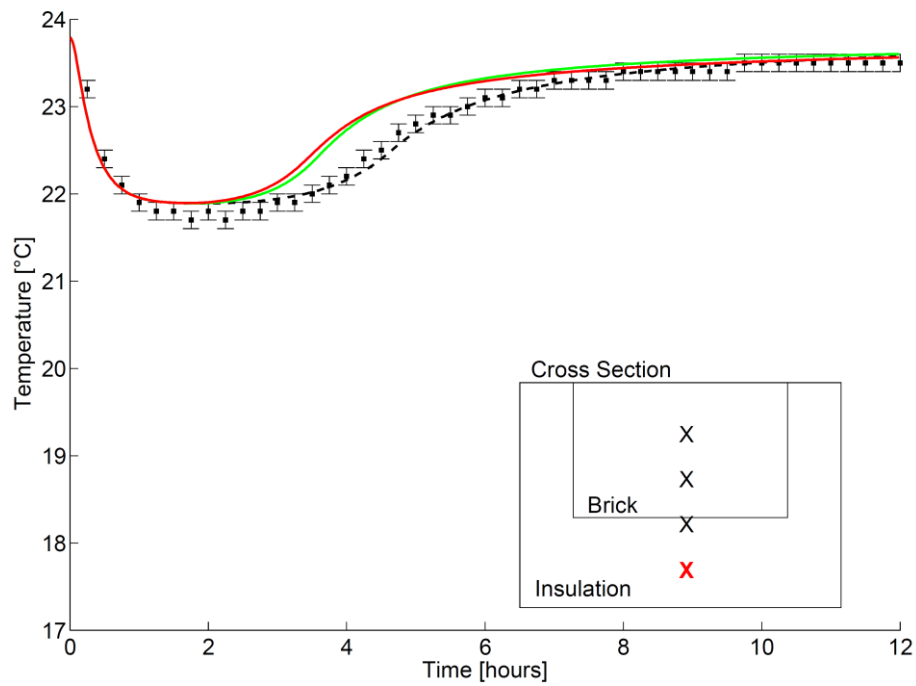


(b) Temperature at 20mm, in brick





(c) Temperature at 30mm, at bottom of brick



(d) Temperature at 40mm, 10mm in insulation

Fig. 6. Comparison between heat and moisture transport model with original material data (- -), model with adjusted retention curve (- - -) and model with adjusted liquid permeability (- - -). Temperature measurement indicated by (\*).

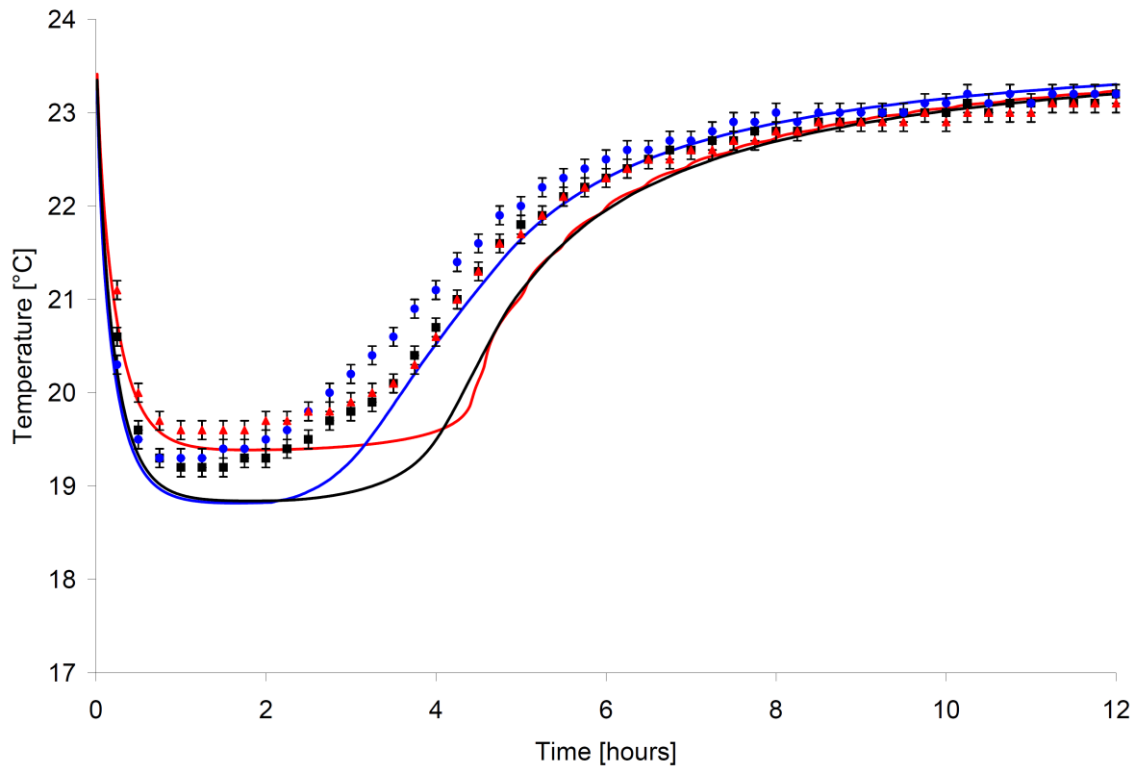


Fig. 7. Simulated temperature in the ceramic brick, upstream of the centre (blue), in the centre (black) and downstream (red). Comparison with measurements upstream (o), centre (□) and downstream (▲).

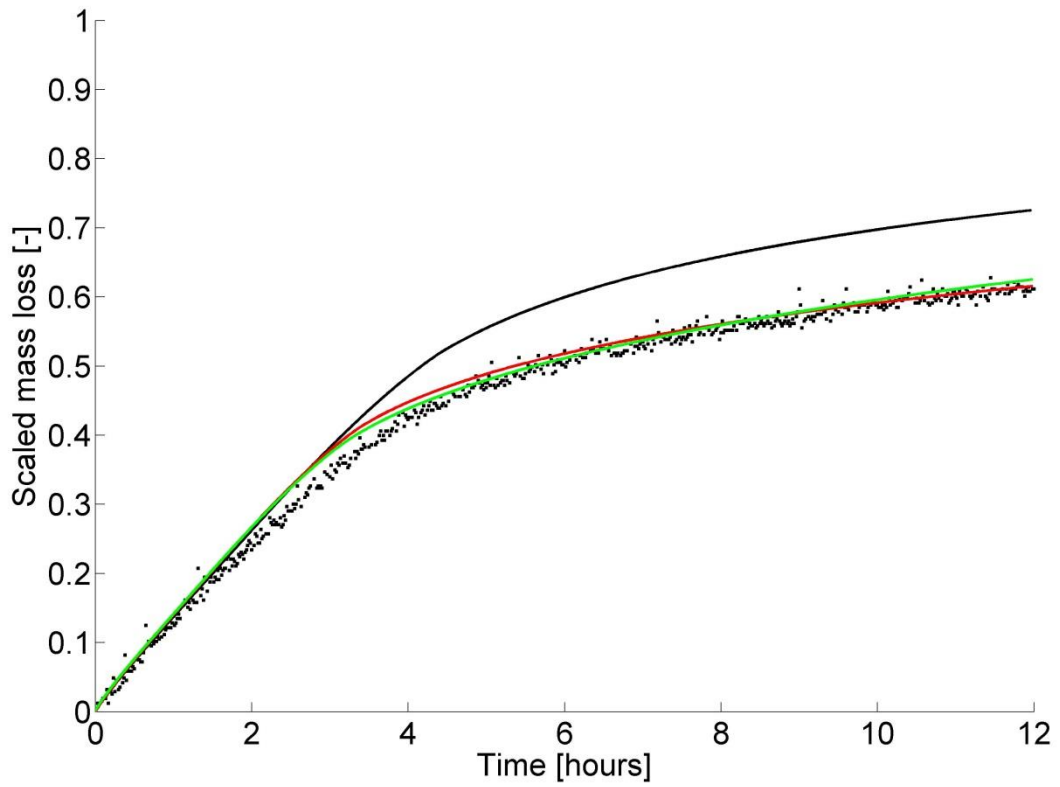
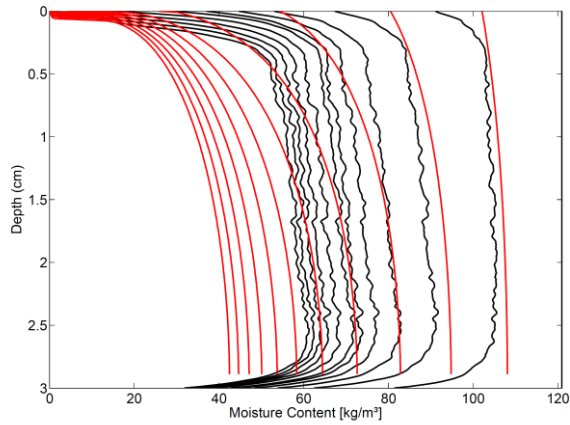
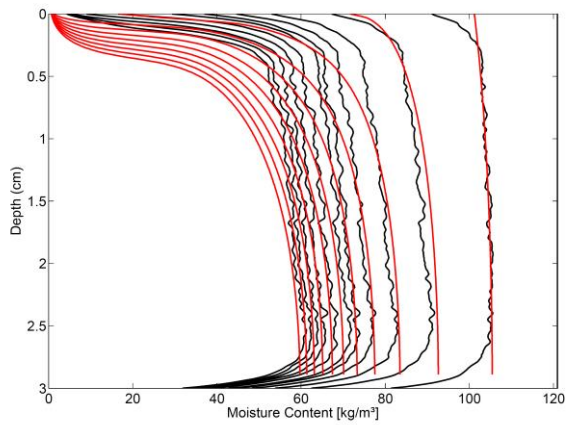


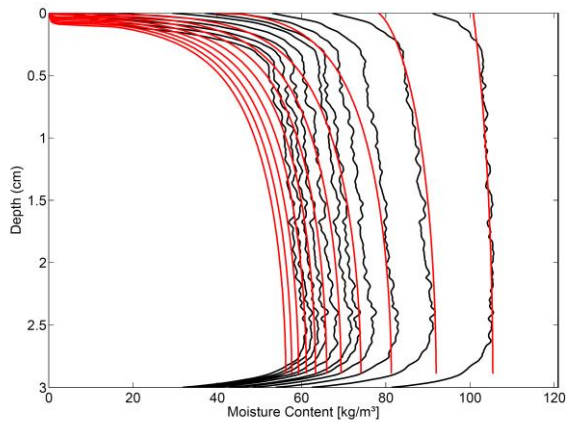
Fig. 8. Scaled mass loss. Comparison of experiment (■), CFD-HAM simulation with original material properties (--) , with adjusted retention curve (-) and adjusted liquid permeability (-).



(a) Moisture distribution when using the original material properties as reported by [46]



(b) Moisture distribution when using an adjusted retention curve



(c) Moisture distribution when using an adjusted liquid permeability

Fig. 9. Comparison of the measured (--) and simulated (--) moisture content distribution in the ceramic brick sample over time. Time difference between two lines is 1 h.

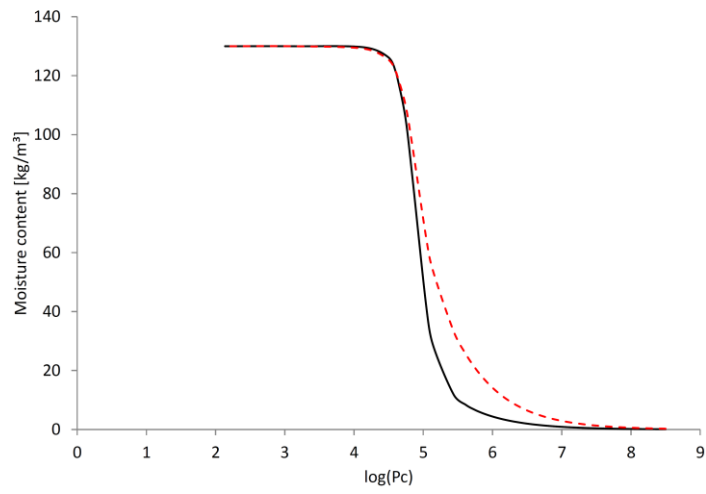


Fig. 10. Retention curve of brick: original curve [45] (--) and adjusted curve (- -).

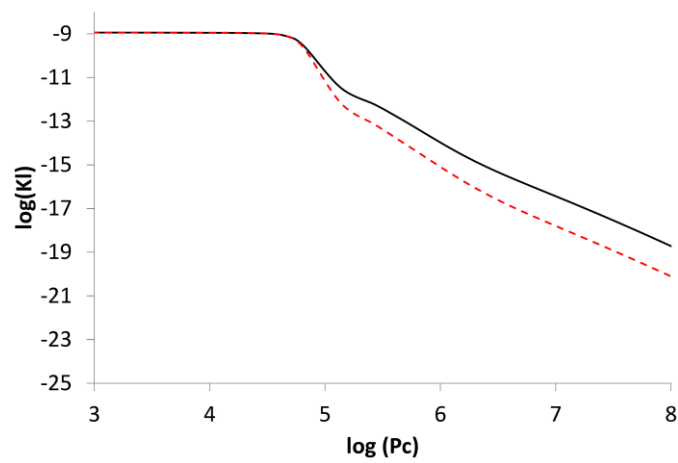


Fig. 11. Liquid permeability of ceramic brick: original curve [45] (--) and adjusted curve (- -).

Table 1. Material properties of ceramic brick [45].

Property	Value
Density $\rho$ [kg/m <sup>3</sup> ]	2087
Thermal conductivity $\lambda$ [W/mK]	$1 + 0.0047 w$
Specific heat $c_p$ [J/kgK]	840
Water vapour resistance diffusion factor $\mu_{dry}$ [-]	24.79
Capillary moisture content $w_{cap}$ [kg/m <sup>3</sup> ]	130
Open porosity $\psi_0$ [-]	0.13

Table 2. Parameters in Eq. (22) [45].

i	1	2	3
$a_i$	1.35e-5	4e-6	5e-7
$n_i$	6	2	0.7
$m_i$	0.8333	2	0.4
$w_i$	0.36	0.25	0.39
$w_i$ adjusted	0.5	0.25	0.25
$K_s$	1.15e-9		
$\tau$	4.003		

Table 3. Standard deviations of material properties as listed by Ref. [50].

Property	Standard deviation
$\rho$	1%
$c_p$	5%
$\lambda$	5%
$\mu_{dry}$	18%
$w_{cap}$	5%
$K_l$	1% on $K_l$ , and 1% on log-log scale